

Chaldeckas, O., Vaks, A., Haviv, I., Gerdes, A., and Albert, R., 2021, U-Pb speleothem geochronology reveals a major ca. 6 Ma uplift phase along the western margin of Dead Sea Transform: GSA Bulletin, <https://doi.org/10.1130/B36051.1>.

## Supplemental Material

**Data File 1.** Activity Ratios

**Data File 2.** U-Pb Chronology

### STUDY SITES

#### ANALYTICAL PROCEDURE

**Table A1.** U-Th analytical results

**Figure A1.** The map of the research area (a) and aerial view Ma'ale Meyshar cave complex (b).

**Figure A2.** Ma'ale Meyshar cave (MMR) and its speleothems (Site #1.1 in Fig. A1-b; 450 m asl).

**Figure A3.** Ma'ale Meyshar small cave 3 (MMRS-3) and speleothems, as seen in outcrop and hand samples (Site #1.2 in Fig. A1-b; 480 m asl).

**Figure A4.** Ma'ale Meyshar small cave 1 (MMRS-1) and speleothems from there (Site #1.3 in Fig. A1-b; 510 m).

**Figure A5.** Ma'ale Meyshar small cave 4 (MMRS-4) and speleothem as seen in hand samples (Site #1.4 in Fig. A1-b; 525 m).

**Figure A6.** Ma'ale Meyshar small cave 5 & 6 (MMRS-5 & 6) and speleothem as seen in core and hand sample (Site #1.5 in Fig. A1-b; 530 m).

**Figure A7.** Ma'ale Meyshar small cave 7 (MMRS-7) (Site #1.6 in Fig. A1-b; 620 m).

**Figure A8.** Ma'ale Meyshar small cave 8 (MMRS-8) (Site #1.7 in Fig. A1-b; 630 m):

**Figure A9.** The estimated drop in groundwater levels in Ma'ale Meshar cave complex - Central Negev (Site #1 in Fig. 1).

**Figure A10.** Barbur cave (BRBC) and speleothems:

**Figure A11.** Ma'ale Deragot Quarry cave (MDRG) (Site #2 in Fig. 1):

**Figure A12.** Schematic cross sections depicting the setup of sites #2 (see Fig. 1) and Barbur cave.

**Figure A13.** Shimshon East cave (SHE) speleothems as seen in-situ and hand sample (Site #3 in Fig. 1):

**Figure A14.** Har-Tuv Quarry cave (HRT) with phreatic speleothems as seen in-situ (Site #3 in Fig. 1, Fig. 10).

**Figure A15.** U-Pb ages obtained from Judean Mountain speleothems- Shimshon East (SHE) and Har-Tuv Quarry (HRT) caves (Site #3, Fig. 1).

**Figure A16.** An example for laser ablation U-Pb thin section analysis.

**Figure A17.**

**Figure A18.**

**Figure A19.** Topographic map of Ma'ale Meyshar showing the spatial relationship between major structural elements and fracture caves (Site #1, Fig. 1, Fig.4, Fig. A1)

**Figure A20.** Distance of cave sites from main water divide.

## STUDY SITES

### Ma'ale Meyshar cave complex

Ma'ale Meyshar cave complex (7 sub-sites) is located on the southeastern flank of Badad anticline, on the footwall of Arif-Batur-Hadav fault (Bartov, 1974; Zilberman, 1983), and 100 – 280 m above Wadi Meyshar, which acts as a local base level which drains the surrounding region through the Meyshar-Neqarot canyon (Site #1 in Figure 1 and Figure A1-a, Figure 4a,b). The site is located 20 km southeast of town of Mitzpe Ramon (Fig. A1-a), within Cenomanian dolomite host rock (Tamar Formation). The system consists of several caves, which can be separated into two major groups (Fig. 4c):

(1) Hypogene chamber caves, similar to those found on western flanks of anticlines of central Israel (Frumkin and Fischhendler, 2005). They lie at elevation of 450 – 510 m asl (Fig. 4c; Sites #1.1 – 1.3 in Figure A1-b), containing phreatic mammillaries and phreatic calcite cave rafts, in some places covered with vadose flowstone (caves *MMR*, *MMRS-3* and *MMRS-1*).

(2) Tectonic caves formed along fractures which lie at elevation of 525 – 630 m asl (Fig. 4c; Sites #1.4 – 1.7 in Figure A1-b), containing only vadose flowstone (caves *MMRS-4-II*, *MMRS-5+6*, *MMRS-7* and *MMRS-8*).

A thin layer of calcite spar crystals, enriched with manganese oxide, precedes all the speleothem layers in this site. In several places, similar deposit is found in veins filling cracks and vugs within the host rock in the vicinity of the caves.

The caves in Ma'ale Meyshar complex are described below from the lowest to the highest cave.

*Ma'ale Meyshar cave (MMR)* (#1.1 in Figure A1-b; Fig. A2) is a hypogene chamber cave 10–12 m in length and up to 2 m in height. It lies at 450 m asl and contains a 7 cm thick mammillaries, which are covered in places by up to 3 cm of vadose flowstone and dripstone.

*Ma'ale Meyshar small cave 3 (MMRS-3)* (#1.2 in Figure A1-b; Fig. A3) is a small hypogene chamber cave (3x2x3 m) at 480 m asl. Phreatic mammillary overgrowth up to 5–6 cm thick coat the cave walls and ceiling. In the lower part of the cave the mammillary overgrowth is covered by a ~0.5 m thick sequence of phreatic cave rafts. Above the rafts, alternating layers of vadose flowstone and sediments up to 21 cm thick are found.

*Ma'ale Meyshar small cave 1 (MMRS-1)* (#1.3 in Figure A1-b; Fig. A4) is a small hypogene chamber cave (2x1x3 m) at 510 m asl. It contains 1 cm thick phreatic mammillary overgrowth, which is, covered in places by flowstone, up to 7 cm thick.

*Ma'ale Meyshar cave 4 (MMRS-4)* (#1.4 in Figure A1-b; Fig. A5) is a tectonic fracture cave located at an elevation of 525 m asl. It is situated along a fracture with a strike of 70°, covered on both sides by flowstone up to 7 cm thick.

*Ma'ale Meyshar caves 5 and 6 (MMRS-5&6)* (#1.5 in Figure A1-b; Fig. A6) is tectonic fracture caves with a strike of 350°, at an elevation of 530 m asl. The both sides of fracture are incrustated by 1 cm of flowstone. *MMRS-6* was collected from the same sequence using a core driller.

*Ma'ale Meyshar cave 7 (MMRS-7)* (#1.6 in Figure A1-b; Fig. A7) is a tectonic fracture cave located at an elevation of 620 m asl with a strike of 90°. It consists of a layer of manganese oxide and calcite spar crystal, covered by sediments with carbonate matrix and flowstone.

*Ma'ale Meysnar cave 8 (MMRS-8)* (#1.7 in Figure A1-b; Fig. A8) is a tectonic fracture cave filled with flowstone deposit and stalactites, up to 7 cm thick on both sides of the fracture. The cave is located at an elevation of 630 m asl with a strike of 10°.

### **Barbur Cave**

*Babur cave (BRBC)* (Figure A1-a) is hypogene chamber cave that was one of the sampling sites in this study. Due to poor preservation of the samples, resulted in only one U-Pb age with large uncertainty the site was not included in the paper. The cave is located 10 km northeast from the town of Dimona (Fig. A1-a), on the southeastern flank of Dia-Dimona anticline, at an elevation of 400 m asl and 50 m above Wadi Dimona. The cave host rock is Turonian limestone (Shivta Formation), and the speleothems include a 5 cm thick phreatic mammillary overgrowth and 0.5 m thick sequence of calcite cave rafts (Fig. A10-b; Fig. A11).

### **Ma'ale Deragot Quarry**

*Ma'ale Deragot Quarry (MDRG -#2)*, Figure 1-a) is located on the southern slopes of the Judean Mountains, and several kilometers north of Beer-Sheva-Arad Valley, which separates the Judean Mountains in the north from the Negev Highlands in the south. The quarry is located on southeastern flank of Kohal-Ira (Ma'on) anticline (Site #2 in Figure 1; Figure A10-a;), within a Turonian limestone host rock (Bina formation), at an elevation of ~600 m asl. The site contains hypogene mini-caves (less than 1 m in diameter) with mammillaries, which are from few cm to several tens of centimeters thick, coated by several tens of cm of vadose flowstone and dripstone. The speleothems sometimes display brecciated morphology (Fig. A12).

### **Judean Mt. caves**

Two sites were sampled in the Judean Mountain area, *Har-Tuv Quarry caves (HRT - #3.1)*, Figure A1-a) and *Shimshon East Cave (SHE - #3.2)*, Figure A1-a). These hypogene chamber caves and mini-caves (less than 1 m in diameter) are located on the western flank of Ramallah anticline, 2 km east of the town of Bet-Shemesh and ~20 km west of Jerusalem within a Cenomanian dolomite host rock at the base of Weradim Formation and above the top of Kefar-Shaul Formation (Site #3 in Figure 1; Fig. 5a). Shimshon East Cave (~430 m asl) and Har-Tuv Quarry Cave (~400 m asl) are located on two opposing hillslopes, separated by the Soreq Valley (~260 m asl) (Fig. 5). The *SHE* cave is completely filled with phreatic mammillaries and was exposed following incision of the Soreq Valley, whereas *HRT* caves were exposed by anthropogenic quarrying. The thickness of the speleothems is ~2 m in *Shimshon East Cave* (Fig. A13) and a few tens of centimeters in *Har-Tuv Quarry Cave* (Fig. A14).

## Types of speleothems used in the study

In this study we utilize four types of calcite speleothem deposits representing both phreatic (Fig. 3b; Figure A2b,c) and vadose (Fig. 3c; Fig. A3d) conditions:

Stalagmites

Flowstone

Mammillaries

Phreatic calcite cave rafts

*Stalagmites* are a type of vadose speleothem. They form when falling droplets impact the floor of a cave, spatter and deposit a coating, which gradually forms a finely layered conical pillar. The shape of this pillar is determined by the deposition rate of calcium carbonate, which is a function of the rate and direction of the flow. The thickest portion of a stalagmite is located directly at the drip point, decreasing toward the margins and forming a quasi-parabolic shape. Deposition of calcite under arid and semi-arid conditions is often highly intermittent and contain hiatuses (Vaks et al., 2006; Ford and Williams, 2007; Vaks et al., 2013a), reflected by thin (few millimeters thick) layers with detrital material which are often white-beige or brown-orange in color.

*Flowstone* is a vadose calcium carbonate deposit, which precipitates from water films, which flow roughly parallel to the host surface and can cover large areas in the cave (Fig. 3c, Figure A3 b,d). Flowstone is more common on surfaces with gentle gradient but can also be found on vertical walls and open fractures. Flowstone is the most common speleothem in caves, can reach a thickness of more than several meters, and can coat surfaces tens of meters downstream from the water source (Ford and Williams, 2007). Since flowstone often covers large areas, it is more sensitive to changes in water supply and deposition environment, and thus may suffer from hiatuses that often integrate detrital material and fragments of rock and broken speleothems.

*Mammillaries* are a subaqueous (phreatic) calcium carbonate deposit, which lack gravitational flow structures, and forms a crust of uniform thickness on the walls, floor, ceiling and any protruding bulge of the cave (Fig. A2 b,c). Phreatic growth can be intermittent and may contain white or beige layers with microcrystalline and detrital materials or even corrosion signs.

*Phreatic calcite cave rafts* are deposits that form on the water table surface, remain at the surface due to the water surface tension (Fig. 2c; Figure A3 c; Figure A11 c) and sink to the bottom of the cave once they become too thick. Cave rafts can grow outwards from the pool edge or from a protruding rock, or precipitate on dust particles. They constitute excellent indicators for the presence a water surface (water-air transition) inside the cave. Although they may also form on the surface of the pools in vadose zone, the cave rafts are considered phreatic if formed the same time with the mamillaries (Fig. AD2-b).

## ANALYTICAL PROCEDURE

### U-Pb LA-ICP-MS geochronology

The thin sections surface was prepared for analysis in an ultra-sonic bath, submerged in Ethanol for 10 min. In situ laser ablation inductively coupled plasma mass-spectrometry (LA-ICP-MS) was used to measure U and Pb isotopes using previously described procedures (Ring and Gerdes, 2016; Hansman et al., 2018; Li et al., 2014; Nuriel et al., 2017). Isotopic

measurements were conducted using a sector field ICP–MS (Thermo Scientific Element 2) coupled to a RESolution S–155 Resonetics with ASI-Coherent 193nm ArF excimer laser head (CompexPro 102), equipped with a two-volume ablation cell (Laurin Technic). Samples were ablated in helium atmosphere (0.4 l/min) and mixed in the ablation funnel with argon (0.980 l/min) and nitrogen (0.04 –0.06 l/min) for signal stabilization. The ICP–MS was set for maximum sensitivity while keeping oxides (UO/U) minimal. Typical ablation spot size of 380  $\mu\text{m}$  was chosen over previously 213  $\mu\text{m}$  rectangular shaped spot for its improved signal stability due to greater ablated volume. Samples were ablated using a fluence of 1.5 J/cm<sup>2</sup> at 14 Hz repetition, producing a penetration depth of 0.5–1  $\mu\text{m/s}$  in the National Institute of Standards and Technology Standard Reference Material-614 (NIST 21 SRM-614).

Each analysis consisted of a 21 second background measurement, followed by a 26-second ablation pulse with ICP-MS measurement and a subsequent 21 second washout. Prior to the measurement, each spot was pre-ablated by 90 pulses to remove any surface contamination. During the analysis, isotopic data of five masses was acquired using a peak-jumping mode: <sup>206</sup>Pb, <sup>207</sup>Pb, <sup>208</sup>Pb, <sup>238</sup>U and <sup>235</sup>U. Analysis was conducted overnight in a fully automated mode. We performed 10 overnight measurement sequences each consisting of 237–598 ablation spots (Fig. A16).

The raw data was corrected by a macro-based MS-Excel<sup>©</sup> spreadsheet (Gerdes and Zeh, 2006; Gerdes and Zeh, 2009). NIST 614 was used as a primary reference material for <sup>207</sup>Pb/<sup>206</sup>Pb and <sup>238</sup>U/<sup>206</sup>Pb inter-element mass bias and instrumental drift corrections. Offsets driven by changes in the plasma conditions, due to matrix effects were corrected using natural calcite sample – WC-1 (Roberts et al., 2017) and ASH–15–D (Nuriel et al., 2020) as secondary reference materials.

### Raw U-Pb geochronological data

Under ideal conditions, the <sup>234</sup>U/<sup>238</sup>U activity ratio (marked as (<sup>234</sup>U/<sup>238</sup>U)) in a clean speleothem sample should measure unity (1.0), indicating that the <sup>238</sup>U and <sup>234</sup>U are in secular equilibrium. However, in most young speleothems this ratio is often different from one, due to excess <sup>234</sup>U. This effect triggers <sup>234</sup>U daughter excess, which unless corrected for, may cause age deviation in younger samples (Richards and Dorale, 2003; Ford and Williams, 2007).

To correct for excess <sup>234</sup>U in our speleothem samples, we assumed an average initial (<sup>234</sup>U/<sup>238</sup>U) ratio of 1.081 based on (<sup>234</sup>U/<sup>238</sup>U) ratios in 904 speleothem samples from the Negev and the Judean Mts dated by U-Th method in former studies (Supplementary Data Excel File 1 – Regional data of initial (<sup>234</sup>U/<sup>238</sup>U) in speleothems, Figure A17). (Frumkin et al., 1999; Grant et al., 2012; Kagan, 2012; Lisker et al., 2010; Vaks et al., 2006; Vaks et al., 2003; Vaks et al., 2010). The locations of the caves where these studies were performed compared to the location of the caves in this study are shown on Figure A18. Corrected ages were calculated using IsoplotR (Vermeesch, 2018), and shown in Table 2. Corrections for excess <sup>234</sup>U affect the ages by less than 1% and are smaller than the associated 2 $\sigma$  uncertainty of each sample.

Raw data of <sup>238</sup>U/<sup>206</sup>Pb and <sup>207</sup>Pb/<sup>206</sup>Pb ratios in all measurements is available in the Supplementary Data Excel File 2 – Raw U-Pb geochronological data.

## U-Th geochronology

U-Th dating was performed on ten samples at the Geological Survey of Israel (eight from central Negev and two from Judean Mt.). Depending on the uranium concentration (Table A1), 70–220 mg of calcite powder was collected along the growth axis of the sample, using a driller (Dremel 4000) equipped with a 0.8–2 mm high-speed cutting bit (Vaks et al., 2006; Vaks et al., 2010; Grant et al., 2012).

The samples were spiked with  $^{229}\text{Th}$ – $^{226}\text{U}$  spike and dissolved in 2 ml 7N  $\text{HNO}_3$  acid. The solution was centrifuged for 10 min at 4500 rpm in order to separate the insoluble residue from the solution. The residue was dissolved using a 5 ml, 1:2 mixture of concentrated HF and  $\text{HNO}_3$  acids, heated in Teflon beaker to 215 °C for 180 min and then evaporated to dryness. Silica was removed by reaction with HF yielding gaseous  $\text{SiF}_4$ . The residues were dissolved in 7M  $\text{HNO}_3$  acid, added to the samples aliquots, dried up and dissolved in 4 ml 7 M  $\text{HNO}_3$  acid.

2 ml of Bio-Rad AG<sup>®</sup> 1X8 200 – 400 mesh resin was added into mini-columns. The columns were cleaned using two washing cycles with solutions of 5 ml 6M HCl acid and three washing cycles with solutions of double distilled water (DDW). The resin in the columns was pre-conditioned to the sample solution by 8 ml of 7M  $\text{HNO}_3$  acid followed by the sample solution to avoid suspension of the resin.

The matrix was removed by passing through the resin two solutions of 2 ml 7M  $\text{HNO}_3$  acid. Thorium was eluted from the column into Teflon beakers by 5ml 6M HCl acid, followed by elution of uranium from the resin, by 5.5 ml 1M double distilled HBr acid. The U and Th solutions were dried at 160 °C, and the residues were dissolved in 0.5 ml double distilled concentrated  $\text{HNO}_3$  acid. The solutions were dried, and the U and Th residues were dissolved in 2.1 ml and 5 ml 0.1M  $\text{HNO}_3$  acid, respectively.

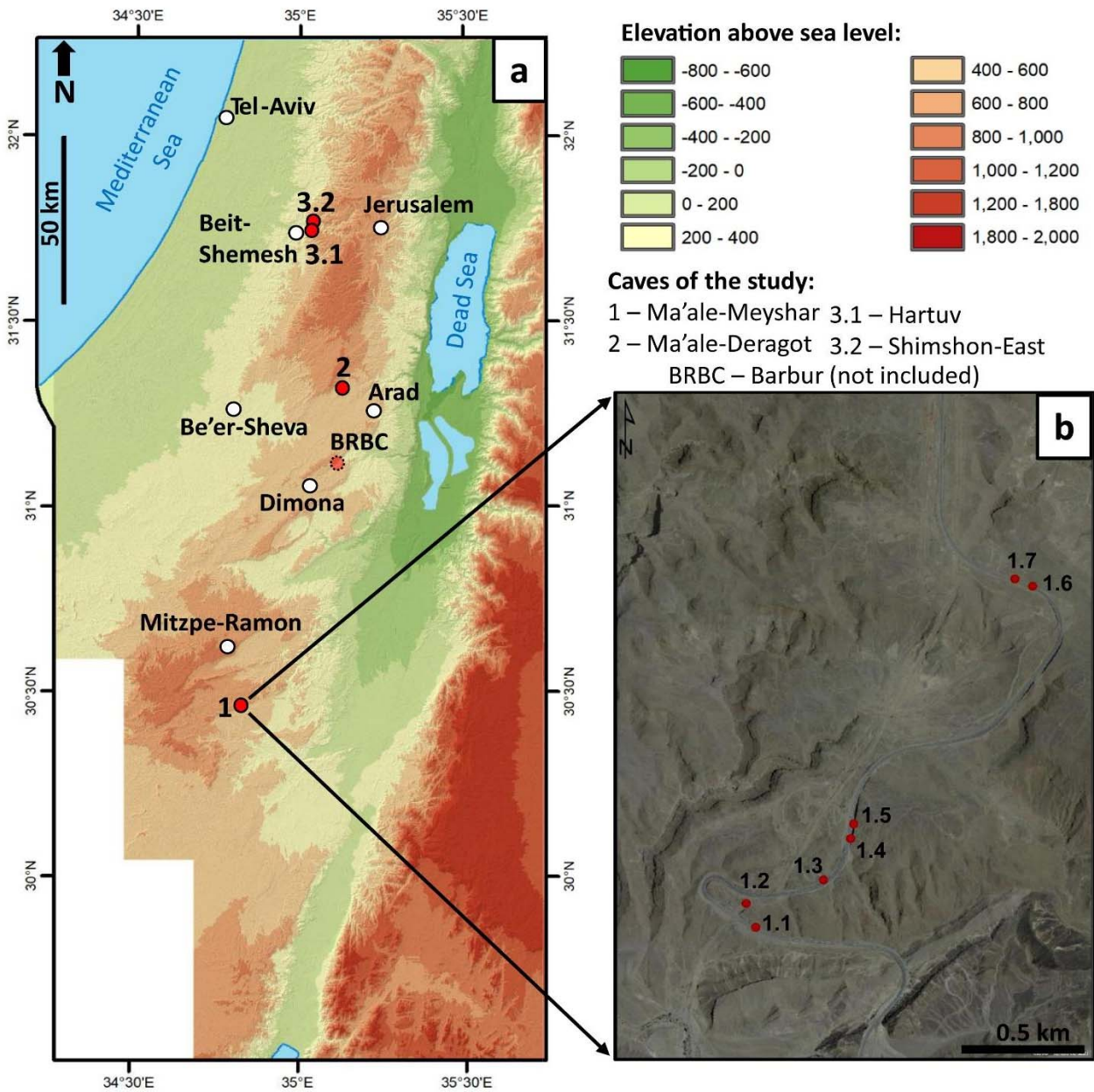
U-Th dating was performed using a Nu Instruments Ltd (UK) multi-collector inductively coupled plasma mass spectrometer (MC-ICP-MS) equipped with 12 Faraday cups and 3 ion counters. Samples were introduced to the MC-ICP-MS through an Aridus<sup>™</sup> micro-concentric desolvating nebulizer sample introducing system. Instrumental mass bias was corrected using an exponential equation by measuring the  $^{235}\text{U}/^{238}\text{U}$  ratio and correcting with the natural  $^{235}\text{U}/^{238}\text{U}$  ratio (137.88). Calibration of the ion counters relative to the Faraday cups was performed using several cycles of measurement with different collector configurations in each particular analysis.

The measured isotope ratios (Table A1) are reported as activity ratios with  $2\sigma$  uncertainties propagated from the run precision errors (0.4% at  $2\sigma$ ), weighing errors and uncertainties in spike concentrations and isotopic compositions.  $^{230}\text{Th}$  and  $^{234}\text{U}$  half-lives follow Cheng et al., (2000). Uncertainties in the half-lives of the U-series isotopes are not included in the error propagation (Vaks et al., 2006; Vaks et al., 2010; Grant et al., 2012).

Table A1. U-Th analytical results

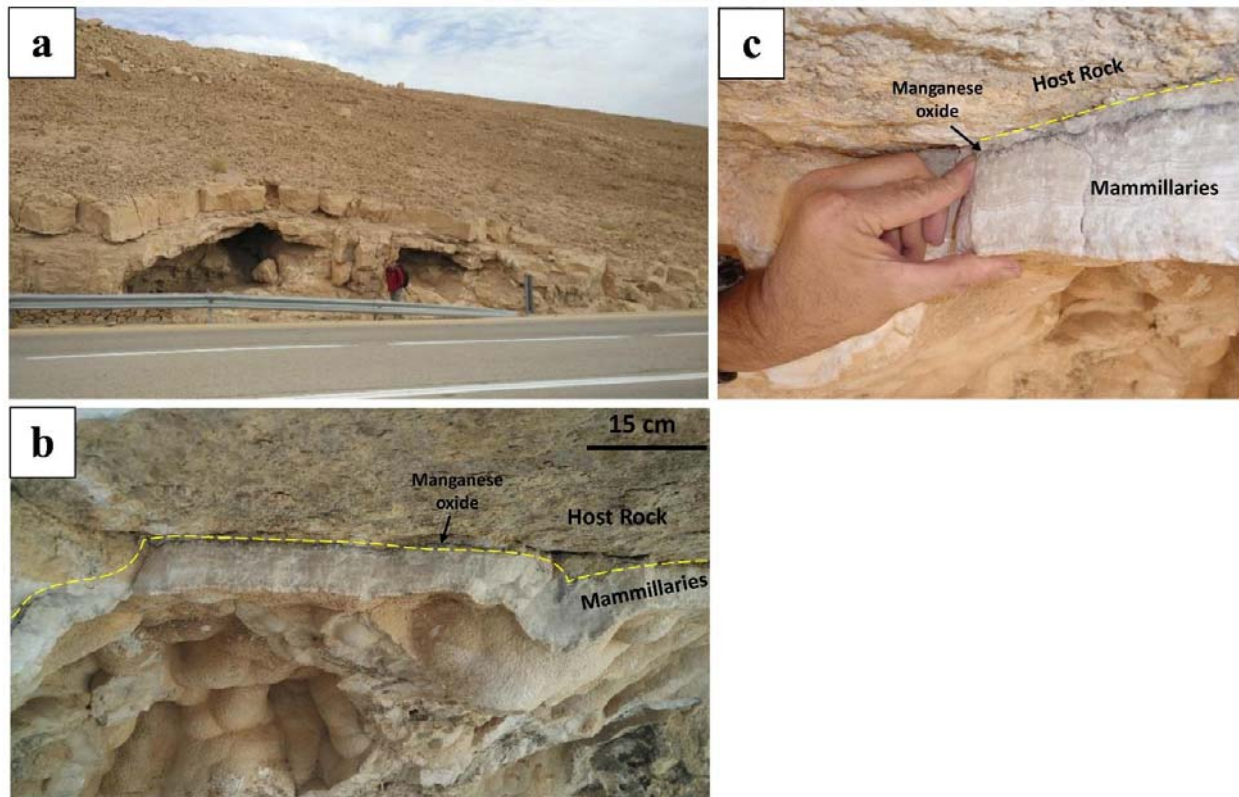
Sample	Lamina	$^{238}\text{U}$ ppm	$^{234}\text{U}/^{238}\text{U}$	$^{230}\text{Th}/^{234}\text{U}$	$^{230}\text{Th}/^{232}\text{Th}$	Age [Ka] $\pm 2\sigma$
MMRS-3-24 TOP SP	A	1.1736	$1.0274 \pm 0.0048$	$0.9011 \pm 0.0057$	157	$244.8 \pm 13.8$
MMRS-3-24 TOP SP	C	0.6459	$1.0105 \pm 0.0022$	$1.0131 \pm 0.0038$	222	> 500
MMRS-3-24	A1	1.0036	$0.9929 \pm 0.0019$	$1.0138 \pm 0.0060$	750	> 500
MMR-31	D	1.5186	$1.0019 \pm 0.0027$	$1.0502 \pm 0.0055$	345	> 500
MMR-31	I	0.2412	$0.9947 \pm 0.0015$	$1.0151 \pm 0.0053$	345	> 500
HT-106		0.5091	$1.1816 \pm 0.0016$	$0.6661 \pm 0.0027$	546	$114.6 \pm 1.7$
SHE-B'	C	0.6430	$1.0068 \pm 0.0019$	$1.0252 \pm 0.0037$	1129	> 500

Figure A1:



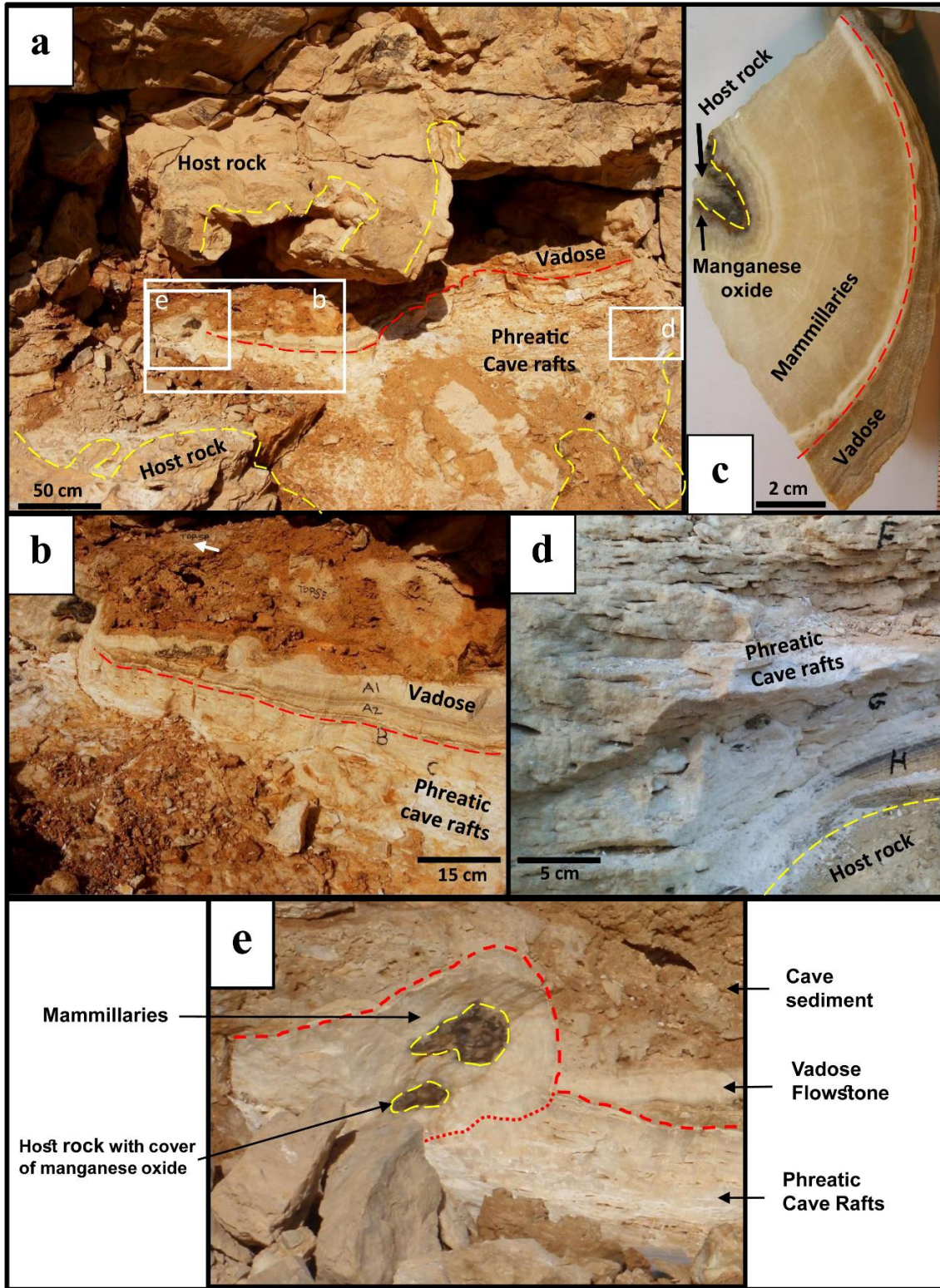
**Figure A1. The map of the research area (a) and aerial view Ma’ale Meyshar cave complex (b).** Ma’ale Meyshar cave complex sampled sub-sites (red circles). **(1.1)** Ma’ale Meyshar Cave (MMR). **(1.2)** Ma’ale Meyshar small cave 3 (MMRS-3). **(1.3)** Ma’ale Meyshar small cave 1 (MMRS-1). **(1.4)** Ma’ale Meyshar small cave 4 (MMRS-4). **(1.5)** Ma’ale Meyshar small cave 5+6 (MMRS-5+6) **(1.6)** Ma’ale Meyshar small cave 7 (MMRS-7) **(1.7)** Ma’ale Meyshar small cave 8 (MMRS-8)

Figure A2:



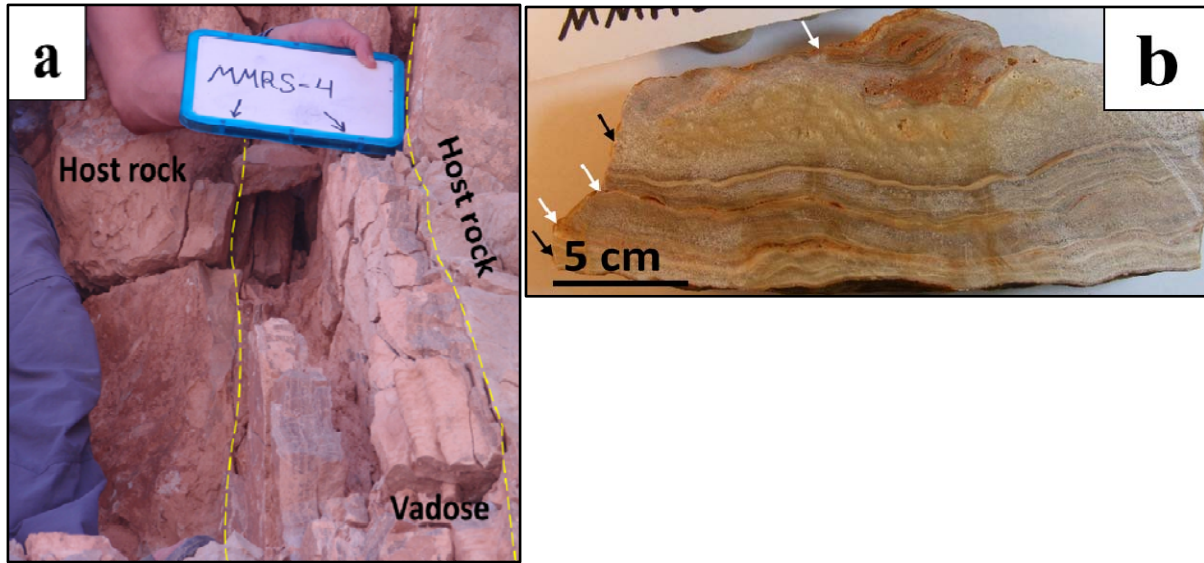
**Figure A2. Ma'ale Meyshar cave (MMR) and its speleothems (Site #1.1 in Figure A1-b; 450 m asl). (a) Ma'ale Meyshar cave. (b) Mammillaries coat the ceiling and the walls of the cave. (c) Enlargement of Figure A2b. The host rock-speleothem transition is marked by dashed yellow line. The base of the speleothem contains a manganese oxide layer, which is typical to phreatic speleothems of Ma'ale Meyshar caves.**

Figure A3:



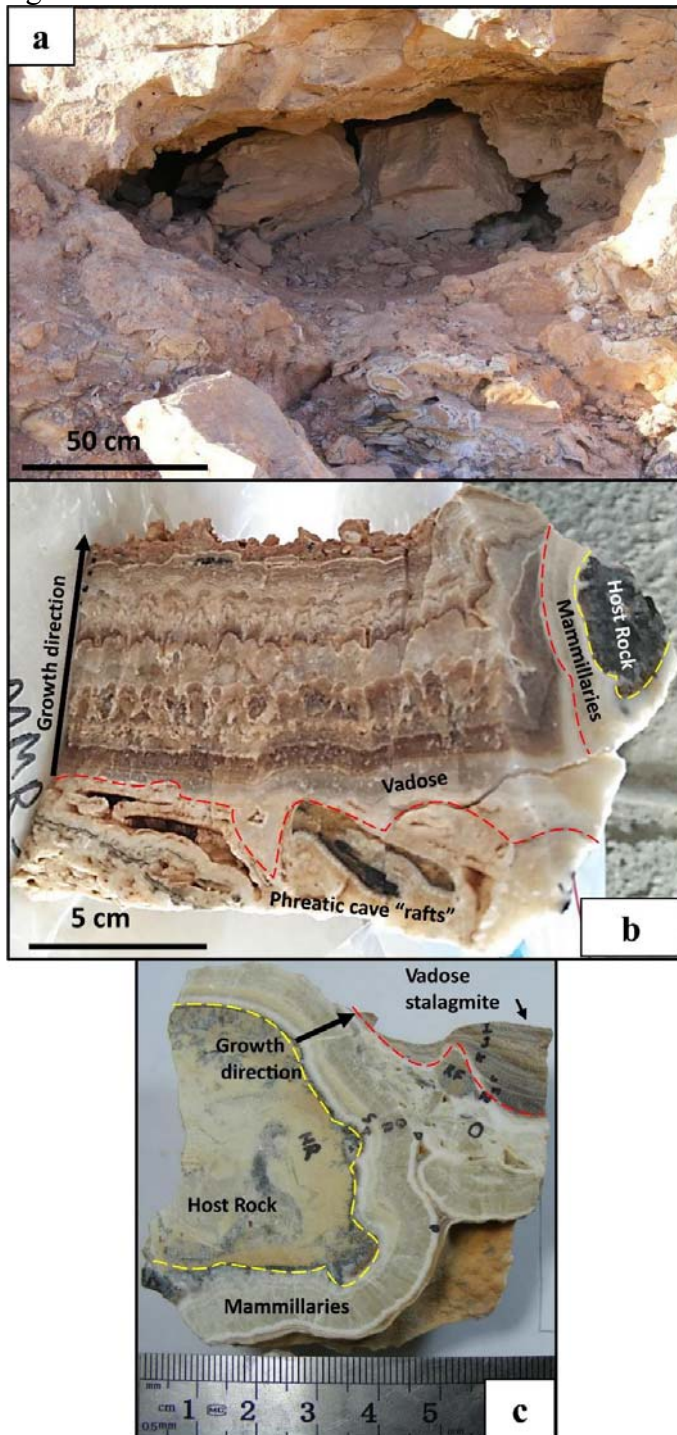
**Figure A3. Ma'ale Meyshar small cave 3 (MMRS-3) and speleothems, as seen in outcrop and hand samples (Site #1.2 in Figure A1-b; 480 m asl).** The host rock-phreatic transition is marked by yellow dashed line. The phreatic-vadose transition is marked by red dashed line. **(a)** Ma'ale Meyshar small cave 3: The cave contains cave rafts (above lower yellow dashed line), covered by vadose flowstone and sediments (above the red dashed line). The ceiling of the cave is covered by mammillaries (below the upper yellow dashed line). **(b)** Enlargement of zone b in sub-figure A3a: The base of the outcrop contains phreatic calcite cave rafts, which are covered by vadose flowstone (above the red dashed line). The flowstone is covered by cave sediments which also contain thin flowstone layers. **(c)** Hand sample composed of host rock fragment, phreatic mammillary overgrowth (right of yellow dashed line), and a vadose flowstone layer (right of red dashed line). The base of the phreatic layer contains manganese oxide, typical to Ma'ale Meyshar cave complex. **(d)** Enlargement of zone c in sub-figure A3-a: A cave rafts layer at the base of the cave, 0.5 m thick. **(e)** Cross-section showing mammillary overgrowth merging into cave rafts layer and layers of vadose speleothems above it.

Figure A4:



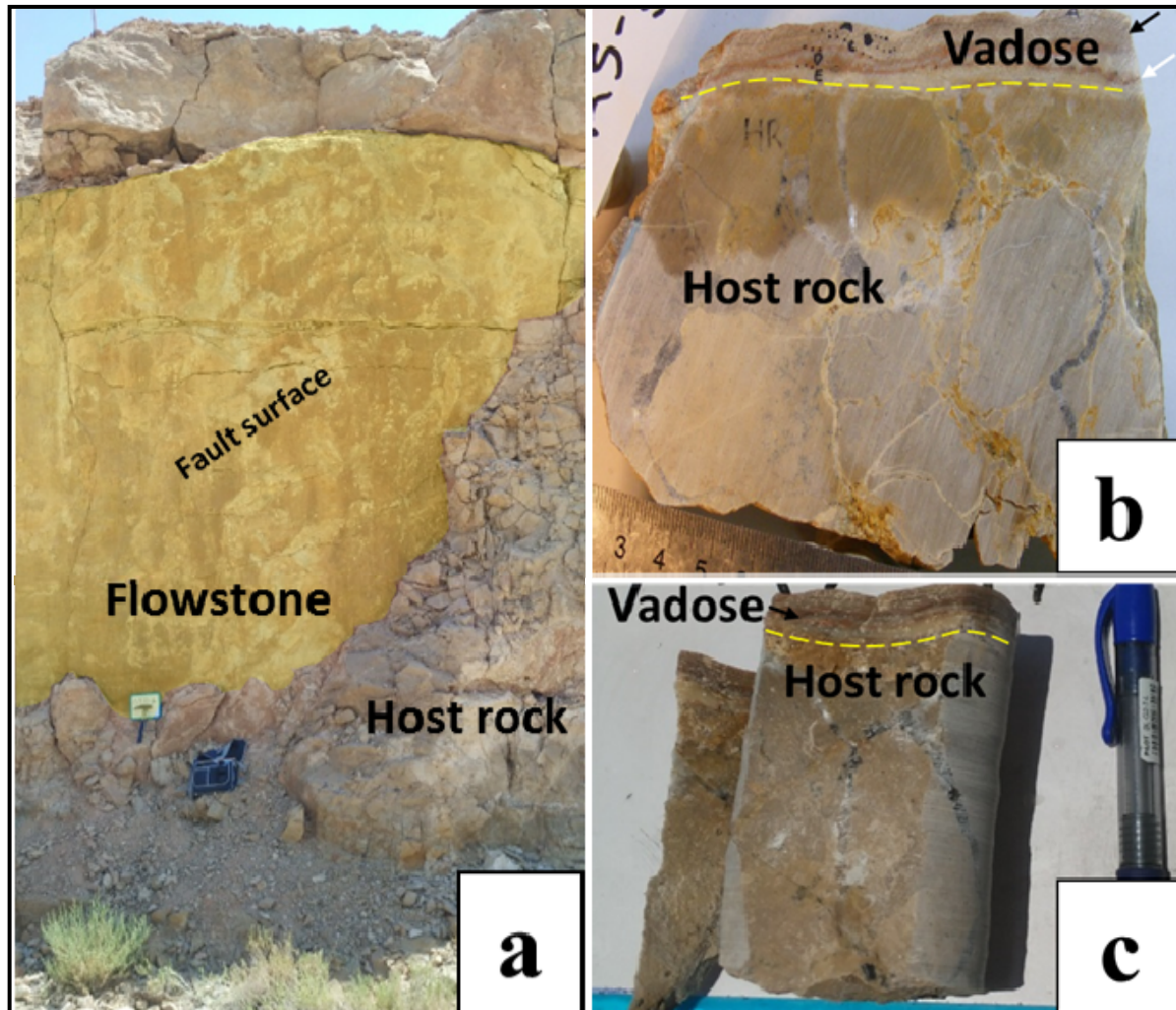
**Figure A4. Ma'ale Meyshar small cave 1 (MMRS-1) and speleothems from there (Site #1.3 in Figure A1-b; 510 m). (a) Ma'ale Meyshar small cave 1 outline. (b) Hand sample composed of host rock (right of yellow dashed line) covered by phreatic overgrowth. The base of the sample contains phreatic calcite cave rafts which are covered by vadose flowstone (above the red dashed line). (c) Hand sample composed of host rock fragment, covered by phreatic mammillary overgrowth (right of yellow dashed line), and by a small vadose stalagmite (above the red dashed line).**

Figure A5:



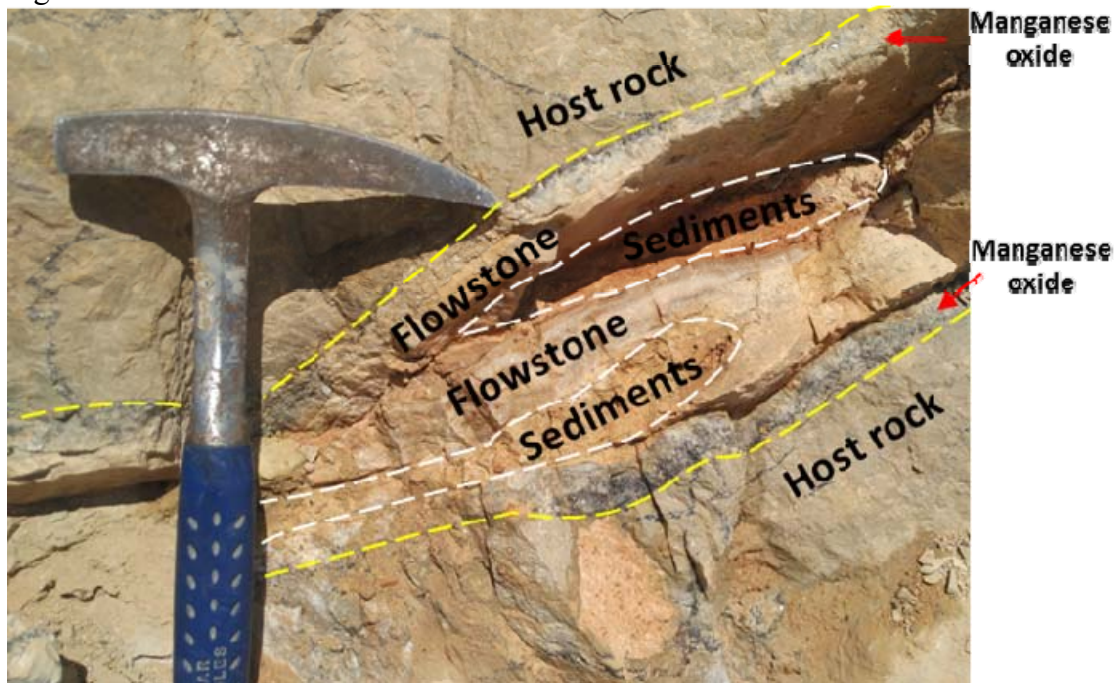
**Figure A5. Ma'ale Meyshar small cave 4 (MMRS-4) and speleothem as seen in hand samples (Site #1.4 in Figure A1-b; 525 m). (a)** Ma'ale Meyshar small cave 4 outline. A tectonic fracture cave filled with vadose flowstone (host rock-flowstone transition marked by yellow dashed line) **(b)** Hand sample composed of alternating layers of yellowish flowstone (black arrow) and brown-beige detrital material, containing mostly clay (white arrows). Detrital layer suggest interruption in deposition or hiatus.

Figure A6:



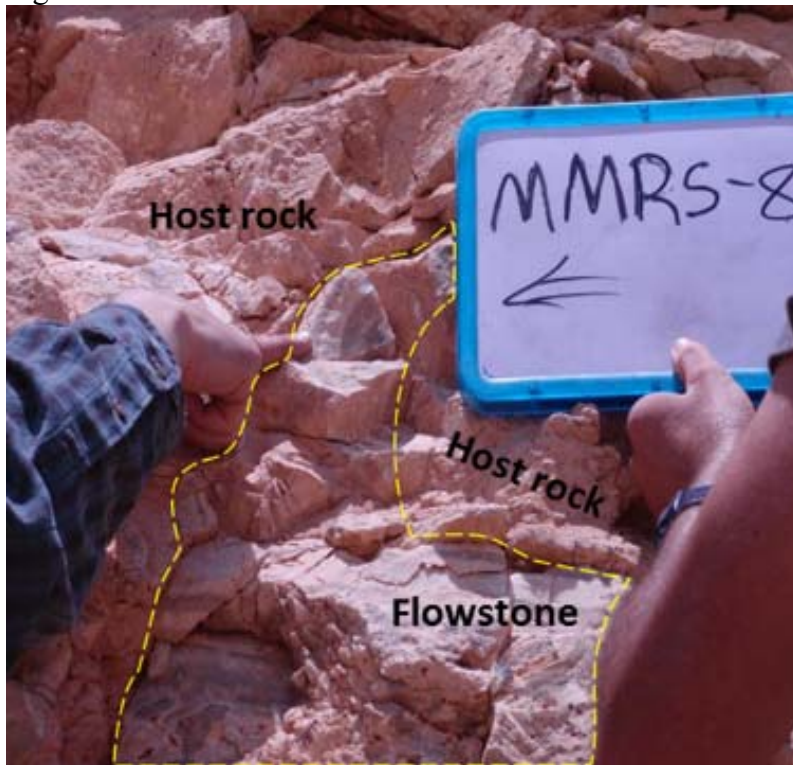
**Figure A6. Ma'ale Meyshar small cave 5 and 6 (MMRS-5 and 6) and speleothem as seen in core and hand sample (Site #1.5 in Figure A1-b; 530 m). (a)** Ma'ale Meyshar small cave 5+6 outline. The cave consists of a tectonic fracture filled with vadose flowstone. A fault surface is highlighted in yellow **(b)** Hand sample composed of alternating layers of yellowish-translucent flowstone (black arrow) and brown-beige detrital material, containing mostly clay (white arrows). Detrital layers might suggest interruption in precipitation or hiatus. **(c)** Core sample taken from the fault surface.

Figure A7:



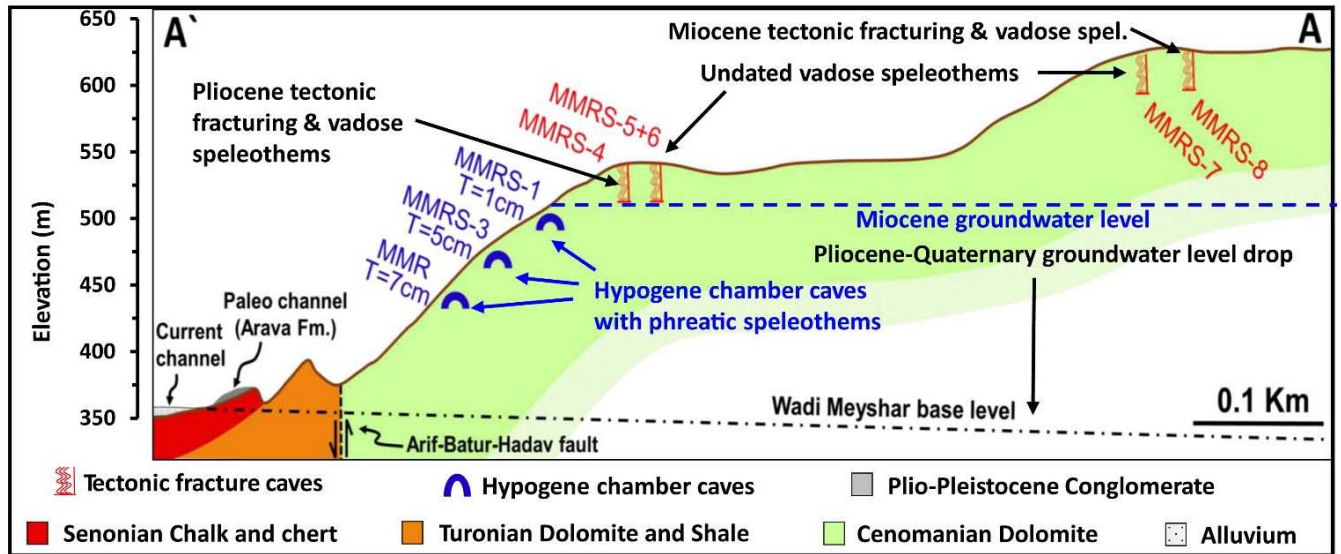
**Figure A7. Ma'ale Meyshar small cave 7 (MMRS-7) (Site #1.6 in Figure A1-b; 620 m).** Ma'ale Meyshar small cave 7 outline. The cave consists of a tectonic fracture and contains a layer of manganese oxide and calcite spar crystal (marked by red arrows), covered by sediments (marked by white dashed line) and flowstone.

Figure A8:



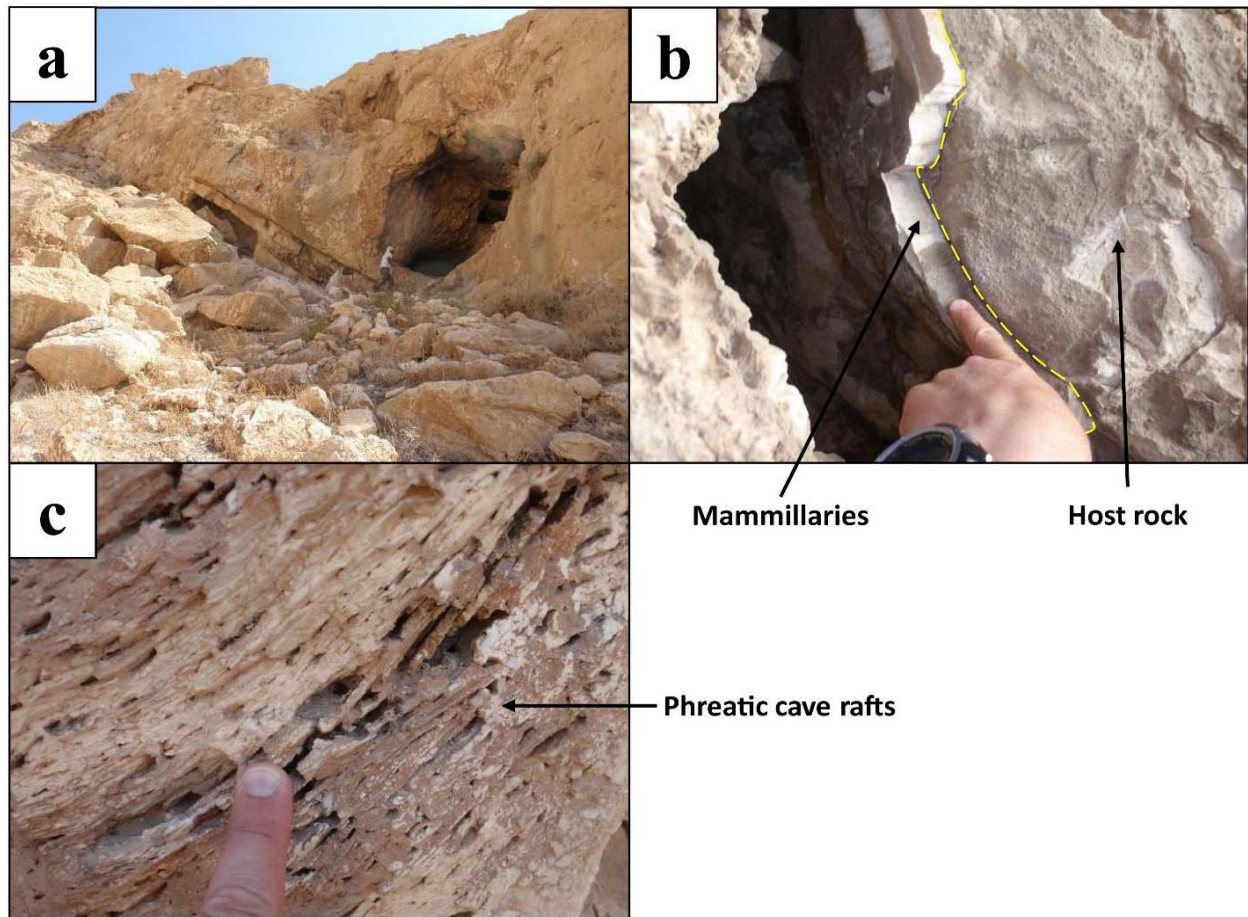
**Figure A8. Ma'ale Meyshar small cave 8 (MMRS-8) (Site #1.7 in Figure A1-b; 630 m): A tectonic fracture cave filled with vadose flowstone (marked by yellow dashed line).**

Figure A9:



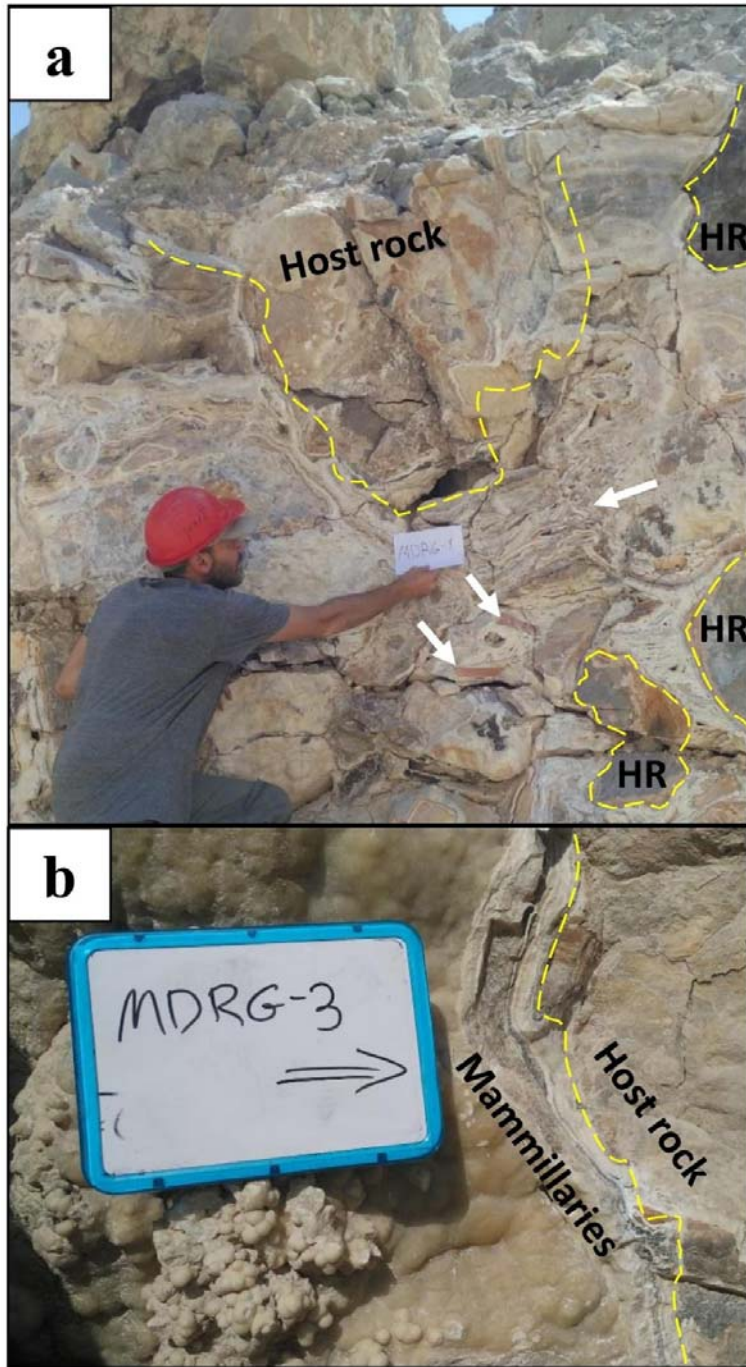
**Figure A9. The estimated drop in groundwater levels in Ma'ale Meshar cave complex - Central Negev (Site #1 in Fig. 1).** U-Pb ages of phreatic speleothem indicate that the groundwater level was at ~510 m asl until the Late Miocene, resulting in deposition of phreatic speleothems below ~510 m asl. Above this level vadose conditions predominated, forming flowstone in open fractures around ~7.5 Ma. A late Miocene decline in the groundwater level triggered deposition of calcite cave rafts at an elevation of 510 m asl. Further decline below 470 m enabled deposition of vadose speleothems in caves between 470 and 510 m asl.

Figure A10:



**Figure A10. Barbur cave (BRBC) and speleothems:** Barbur cave was excluded from this paper due to poor samples' preservation resulting in only one U-Pb age determination with large uncertainty. **(a)** Outline of Barbur cave (BRBC). Note the plunge of Dia-Dimona anticline. The cave contains a sequence phreatic cave rafts and mammillaries encrusting the walls. **(b)** Layer of mammillaries on the wall and ceiling of the cave. Host rock-mammillaries transition is marked by yellow dashed line. **(c)** Sequence of phreatic cave rafts in the cave.

Figure A11:



**Figure A11. Ma'ale Deragot Quarry cave (MDRG) (Site #2 in Fig. 1): (a)** Outline of Ma'ale Deragot Quarry cave (MDRG). Note the brecciated morphology of the speleothems. Speleothem fragments (white arrows) enclosed by younger deposition. Host rock (HR) is marked in yellow dashed line. **(b)** Mammillaries on the wall of the cave. The host rock-phreatic transition is marked by yellow dashed line.

Figure A12:

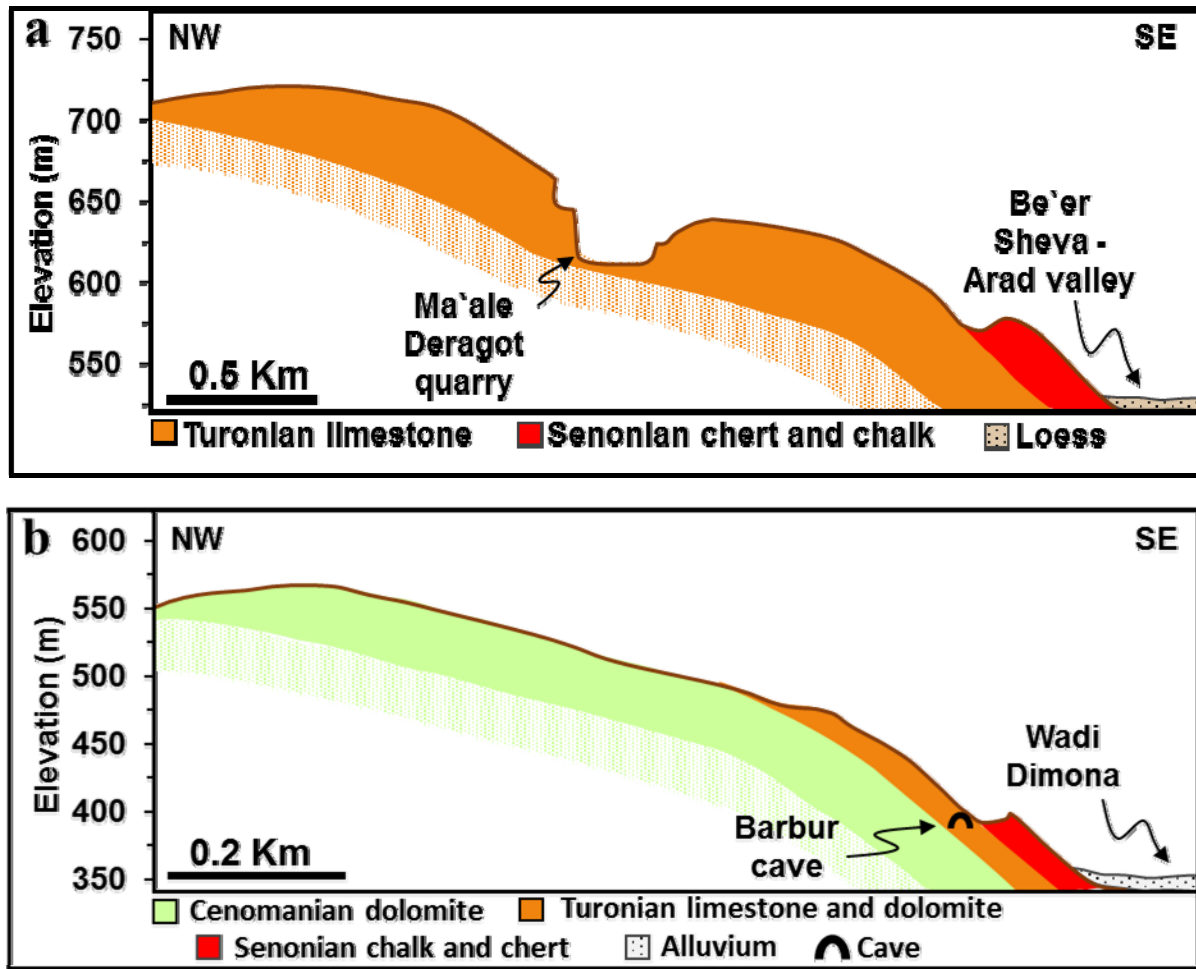
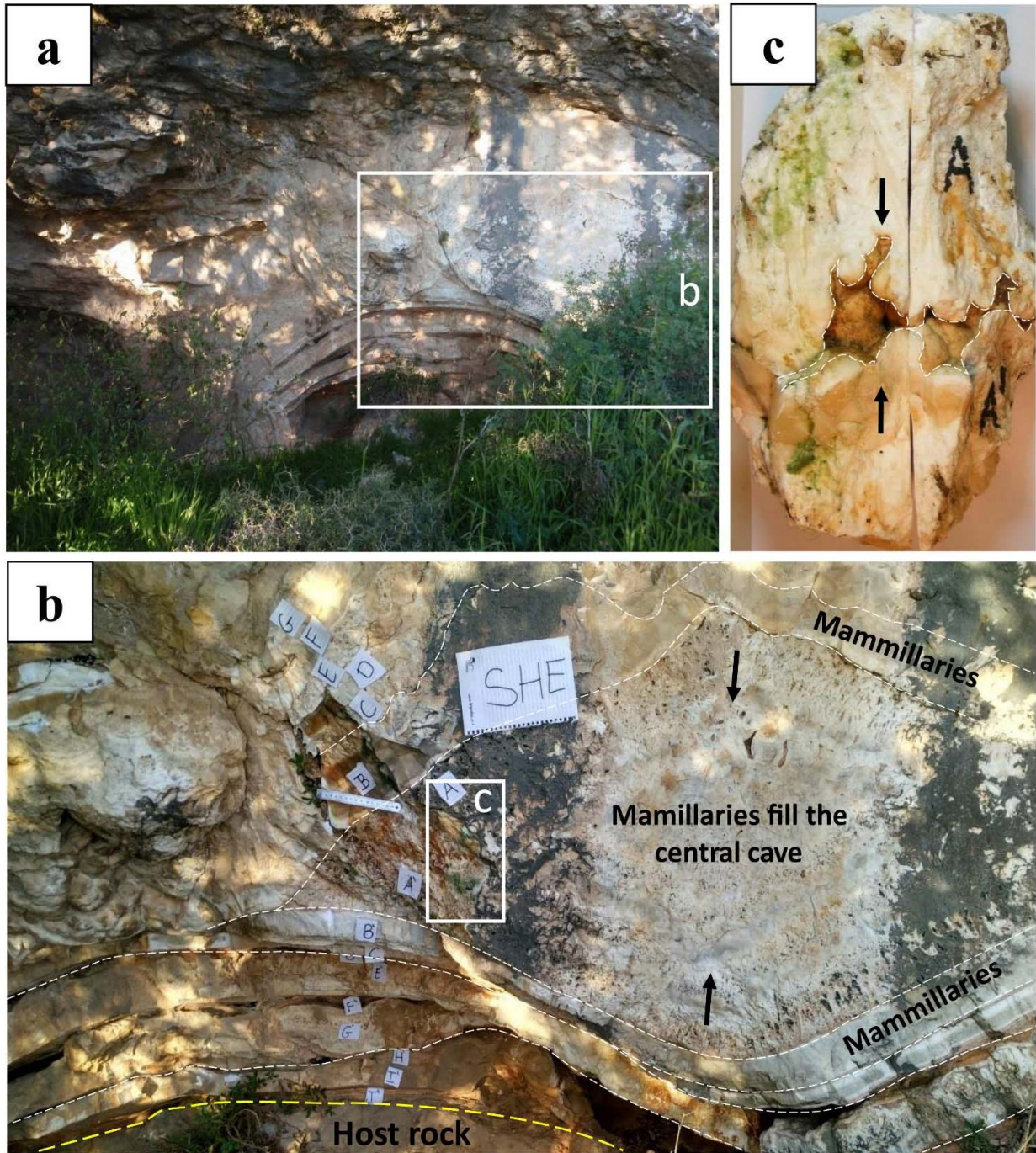


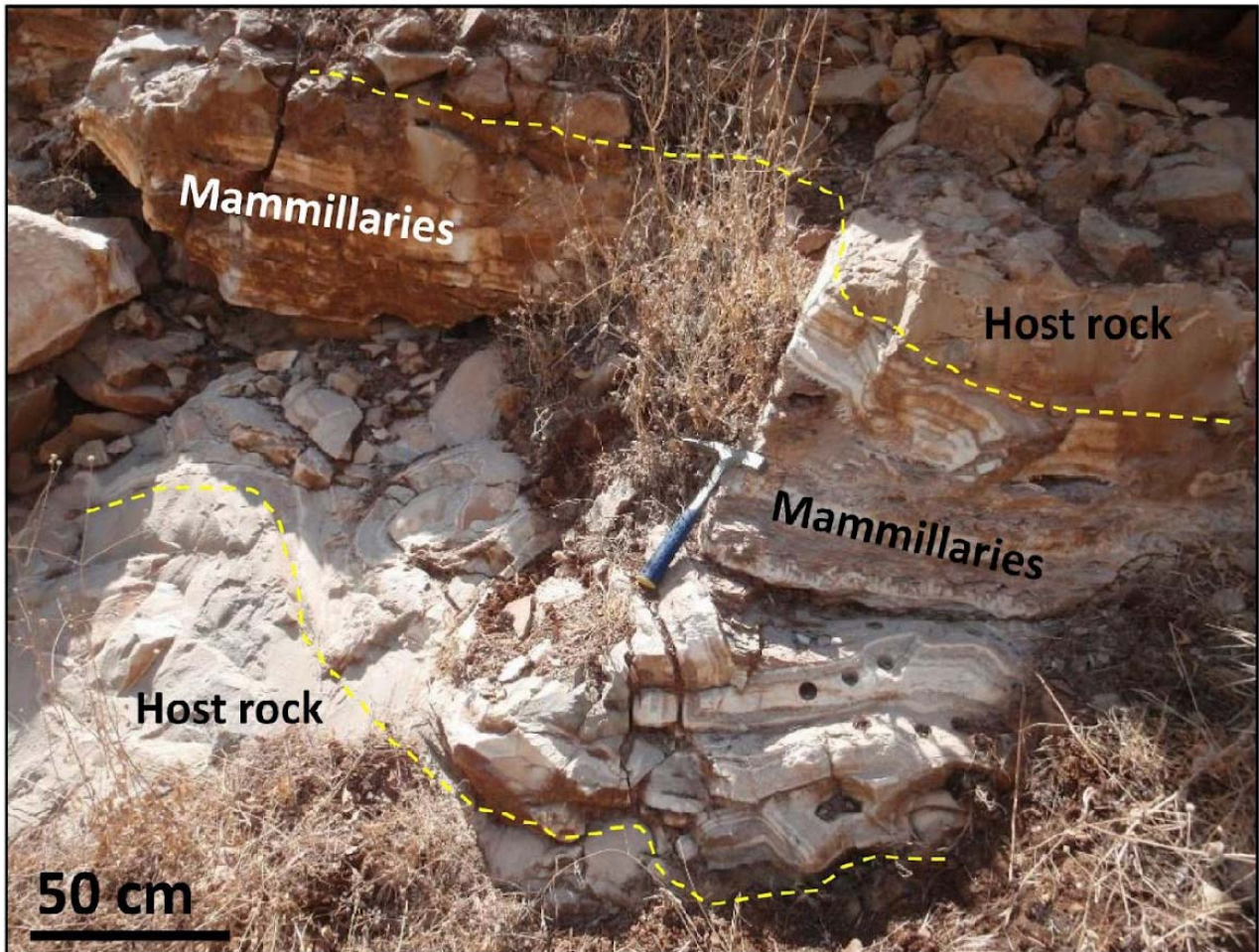
Figure A12. Schematic cross sections depicting the setup of sites #2 (see Fig. 1) and Barbur cave. (a) Schematic cross section depicting the location of Ma'ale Deragot Quarry along the Kohal-Ira anticline. (d) Schematic cross section depicting the location of Barbur cave located along the southeast flank of Dia-Dimona anticline, 50 m above Wadi Dimona.

Figure A13:



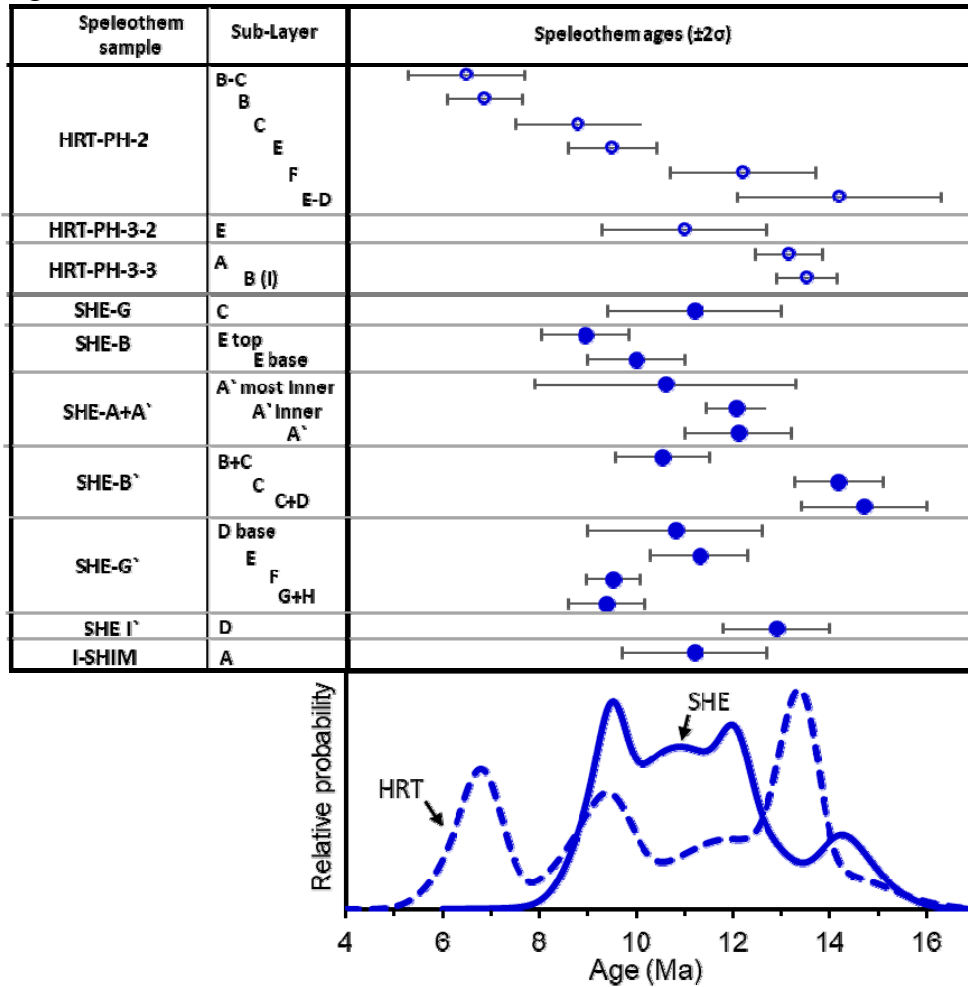
**Figure A13. Shimshon East cave (SHE) speleothems as seen in situ and hand sample (Site #3 in Fig. 1): (a) Shimshon East cave outline. (b) Enlargement of zone b in Figure A13-a. Shimshon East cave consist of a cavern completely filled with mammillaries. The layers grew inward (growth direction marked by black arrows) from the walls and floor (marked by yellow dashed line). Growth layers can be seen (marked by fine white dashed line). (c) Hand sample taken from zone C in Figure A13-b, representing the final growth stage, in which mamillaries fill the remaining chamber from all directions.**

Figure A14:



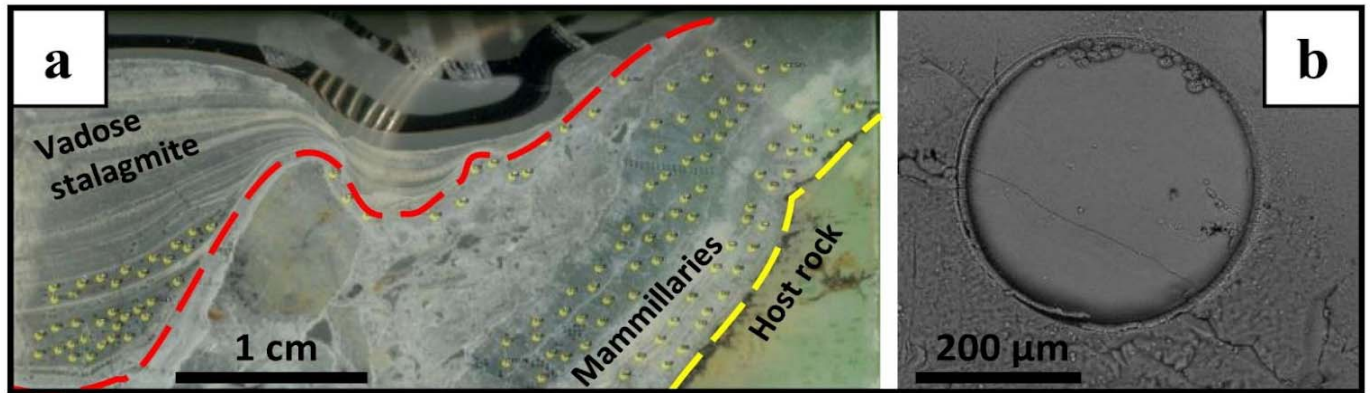
**Figure A14. Har-Tuv Quarry cave (HRT) with phreatic speleothems as seen in situ (Site #3 in Figure 1, Fig. 10).** The quarry contains several caverns filled with phreatic and vadose speleothems. On the picture, one of these caverns can be seen, filled almost completely with mamillaries.

Figure A15:



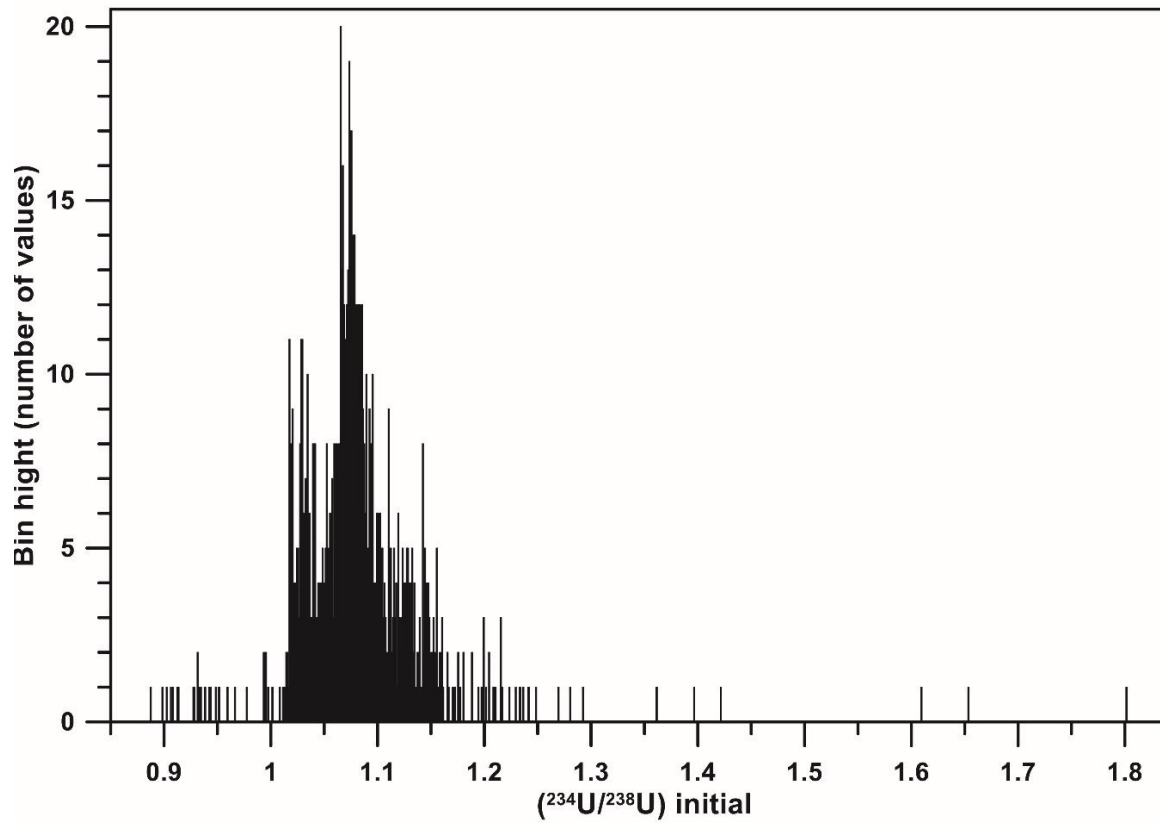
**Figure A15.** U-Pb ages obtained from Judean Mountain speleothems- Shimshon East (SHE) and Har-Tuv Quarry (HRT) caves (Site #3, Fig. 1). **(a)** U-Pb age distribution of speleothem deposition in Har-Tuv Quarry cave (hollow circles) and Shimshon East cave (filled circles) (Site #3 in Fig. 1). The horizontal axis marks the age (Ma). HRT and SHE ages are arranged vertically according to their speleothem sample number and by sub-layer stratigraphy (see Figure A13, A14). Blue circles with error bars define individual age measurement ( $2\sigma$ ). **(b)** Relative probability curve of HRT (dashed blue curve) and SHE (solid blue curve) speleothems ages.

Figure A16:



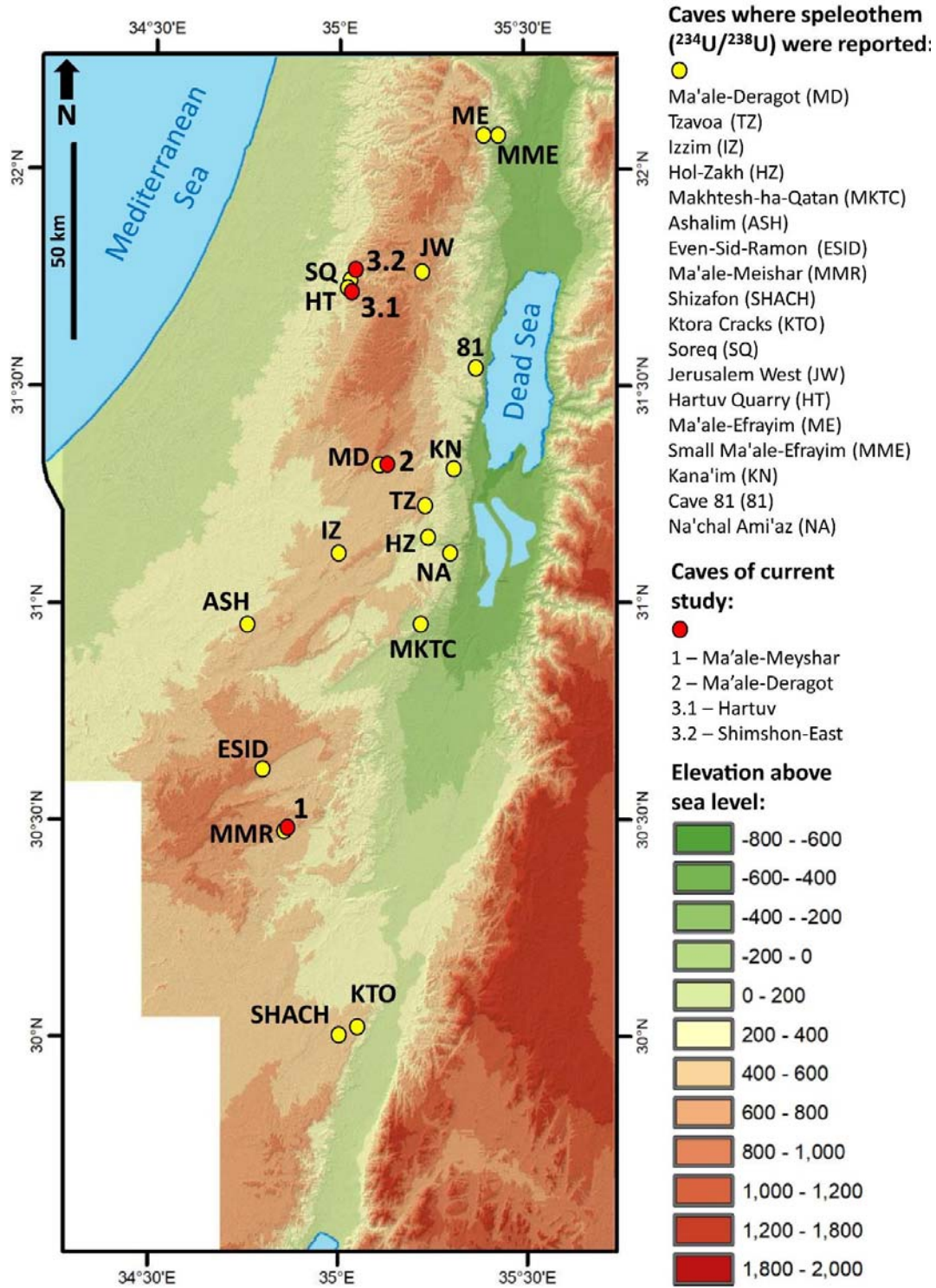
**Figure A16. An example for laser ablation U-Pb thin section analysis. (a)** View of a thick section during pre-scan analysis and ablation spot assignment. The thin section is composed of host rock base (right of yellow dashed line), crust of thin mamillaries (left of yellow dashed line) and vadose stalagmite base (left of red dashed line). Ablation spots are marked by yellow. **(b)** Scanning Electron Microscope (SEM) image of an ablation hole made in a calcite sample during analysis.

Figure A17:



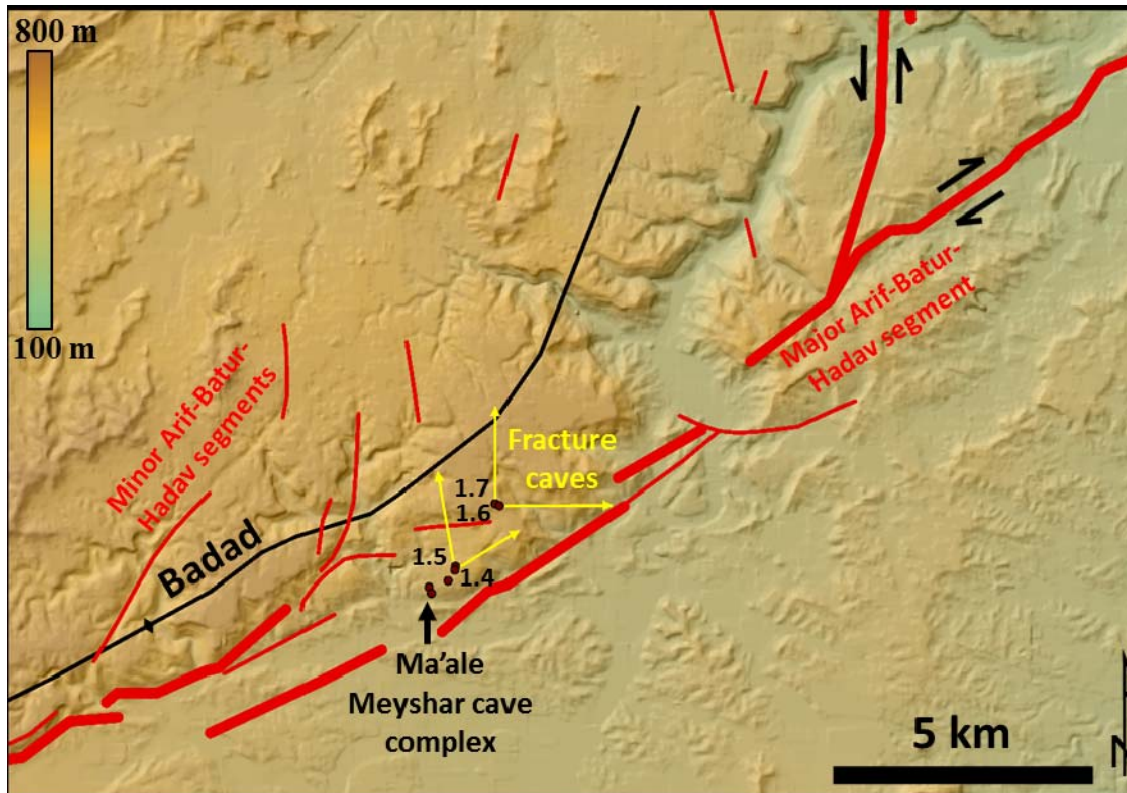
**Figure A17.** Distribution of the initial ( $^{234}\text{U}/^{238}\text{U}$ ) values of 904 dated speleothem samples (Frumkin et al., 1999; Grant et al., 2012; Kagan, 2012; Lisker et al., 2010; Vaks et al., 2006; Vaks et al., 2003; Vaks et al., 2010) in Supplementary Data Excel File 1 – Regional data of initial ( $^{234}\text{U}/^{238}\text{U}$ ) in speleothems.

Figure A18:



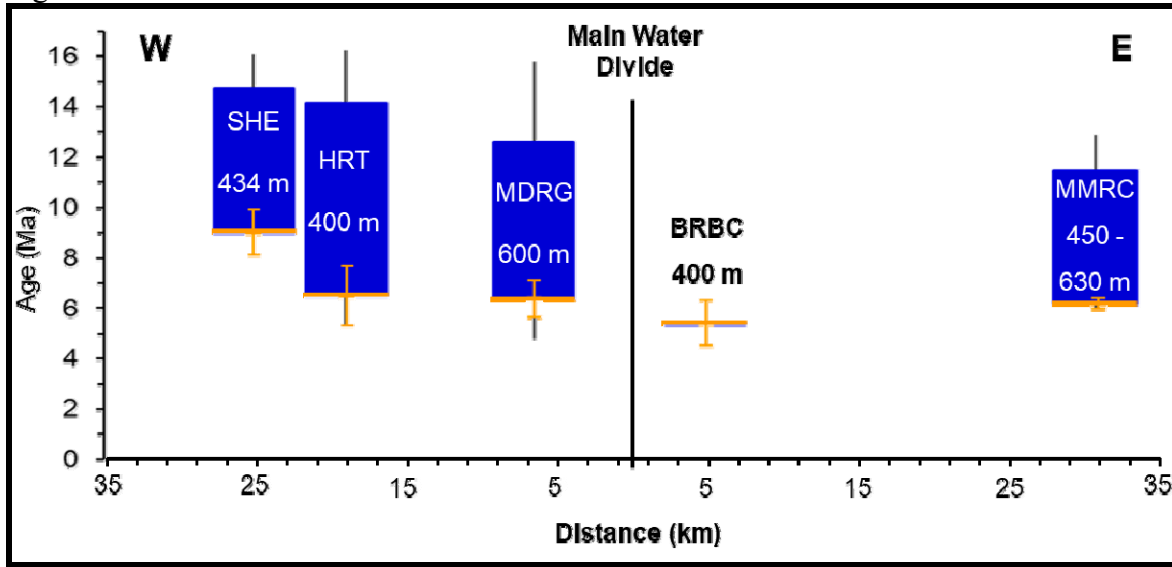
**Figure A18.** The location of the caves where the studies dating the 904 speleothems from Figure A17 and Supplementary Data Excel File 1 were performed (yellow circles), compared with the sites of present study (red circles).

Figure A19:



**Figure A19. Topographic map of Ma'ale Meyshar showing the spatial relationship between major structural elements and fracture caves (Site #1, Figure 1, Figure 4, Fig. A1).** Major and minor Arif-Batur-Hadav fault segments are marked by thick and thin red lines respectively. The main structural elements associated with the 'Syrian arc' fold belt are marked in black line. Ma'ale Meyshar caves are marked by dark red circles. Strike direction of tectonic fracture caves (*MMRS-8* (#1.7), *MMRS-7* (#1.6), *MMRS-5&6* (#1.5), *MMRS-4* (#1.4)) is marked by yellow arrows. Opening of tectonic fracture caves is most probably related to deformation along the Arif-Batur-Hadav major segments (thick red line), the bifurcation point in the northeast and the associated minor fault segments (thin red lines) oriented north-northeast.

Figure A20:



**Figure A20. Distance of cave sites from main water divide.** Horizontal distance from the main water divide and phreatic speleothems deposition period in the cave sites. Elevation of caves is marked in white. The speleothems' deposition period at each site is marked by a blue rectangle, while the bars account for  $2\sigma$  errors. Age of last phreatic deposition at each site is marked by yellow line and associated error ( $2\sigma$ ). Note how phreatic speleothems deposition ceased rather simultaneously in the caves at  $\sim 6$  Ma, regardless to their distance from the main water divide or their elevation. (Barbur cave was excluded from the paper due to poor samples' preservation, resulting in only one U-Pb age with large uncertainty.)

## REFERENCES CITED

- Bartov, J., 1974, A structural and paleogeographical study of the central Sinai faults and domes [Doctoral dissertation]: Hebrew University, Jerusalem.
- Cheng, H., Edwards, R.L., Hoff, J., Gallup, C.D., Richards, D.A., and Asmerom, Y., 2000, The half-lives of uranium-234 and thorium-230: *Chemical Geology*, v. 169, 17 p.
- Ford, D.C., and Williams, P.W., 2007, Karst hydrogeology and geomorphology: Chichester, John Wiley & Sons, 562 p, <https://doi.org/10.1002/9781118684986>.
- Frumkin, A., and Fischhendler, I., 2005, Morphometry and distribution of isolated caves as a guide for phreatic and confined paleohydrological conditions: *Geomorphology*, v. 67, p. 457–471, <https://doi.org/10.1016/j.geomorph.2004.11.009>.
- Frumkin, A., Ford, D.C., and Schwarcz, H.P., 1999, Continental Oxygen Isotopic Record of the Last 170,000 Years in Jerusalem: *Quaternary Research*, v. 51, p. 317–327, <https://doi.org/10.1006/qres.1998.2031>.
- Gerdes, A., and Zeh, A., 2006, Combined U–Pb and Hf isotope LA-(MC-)ICP-MS analyses of detrital zircons: Comparison with SHRIMP and new constraints for the provenance and age of an Armorican metasediment in Central Germany: *Earth and Planetary Science Letters*, v. 249, p. 47–61.
- Gerdes, A., and Zeh, A., 2009, Zircon formation versus zircon alteration—New insights from combined U–Pb and Lu–Hf in-situ LA-ICP-MS analyses, and consequences for the interpretation of Archean zircon from the Central Zone of the Limpopo Belt: *Chemical Geology*, v. 261, 230 p.
- Grant, K.M., Rohling, E.J., Bar-Matthews, M., Ayalon, A., Medina-Elizalde, M., Ramsey, C.B., Satow, C., and Roberts, A.P., 2012, Rapid coupling between ice volume and polar temperature over the past 150,000 years: *Nature*, v. 491, p. 744, <https://doi.org/10.1038/nature11593>.
- Hansman, R.J., Albert, R., Gerdes, A., and Ring, U., 2018, Absolute ages of multiple generations of brittle structures by U–Pb dating of calcite: *Geology*, v. 46, no. 3, p. 207–210, <https://doi.org/10.1130/G39822.1>.
- Kagan, E.J., 2012. Multi-site Quaternary paleoseismology along the Dead Sea Rift: Independent recording by lake and cave sediments, Institute of Earth Sciences: Jerusalem, Israel, Hebrew University of Jerusalem, p. 321.
- Li, Q., Parrish, R.R., Horstwood, M.S.A., and McArthur, J.M., 2014, U–Pb dating of cements in Mesozoic ammonites: *Chemical Geology*, v. 376, p. 76, <https://doi.org/10.1016/j.chemgeo.2014.03.020>.
- Lisker, S., Vaks, A., Bar-Matthews, M., Porat, R., and Frumkin, A., 2010, Late Pleistocene palaeoclimatic and palaeoenvironmental reconstruction of the Dead Sea area (Israel), based on speleothems and cave stromatolites: *Quaternary Science Reviews*, v. 29, p. 1201–1211, <https://doi.org/10.1016/j.quascirev.2010.01.018>.
- Nuriel, P., Weinberger, R., Kylander-Clark, A.R.C., Hacker, B.R., and Craddock, J.P., 2017, The onset of the Dead Sea transform based on calcite age-strain analyses: *Geology*, v. 45, p. 587–590, <https://doi.org/10.1130/G38903.1>.
- Nuriel, P., Wotzlaw, J.F., Ovtcharova, M., Vaks, A., Stremtan, C., Šála, M., Roberts, N.M.W., and Kylander-Clark, A.R.C., 2020, The use of ASH-15 flowstone as a matrix-matched reference material for laser-ablation U–Pb geochronology of calcite: *Geochronology*, v. 3, p. 35–47.

- Richards, D.A., and Dorale, J.A., 2003, Uranium-series chronology and environmental applications of speleothems: *Reviews in Mineralogy and Geochemistry*, v. 52, no. 1, p. 407–460, <https://doi.org/10.2113/0520407>.
- Ring, U., and Gerdes, A., 2016, Kinematics of the Alpenrhein-Bodensee graben system in the Central Alps: Oligocene/Miocene transtension due to formation of the Western Alps arc: *Tectonics*, v. 35, no. 6, p. 1367–1391, <https://doi.org/10.1002/2015TC004085>.
- Roberts, N.M.W., Rasbury, E.T., Parrish, R.R., Smith, C.J., Horstwood, M.S.A., and Condon, D.J., 2017, A calcite reference material for LA-ICP-MS U-Pb geochronology: *Geochemistry Geophysics Geosystems*, v. 18, no. 7, p. 2807–2814, <https://doi.org/10.1002/2016GC006784>.
- Vaks, A., Bar-Matthews, M., Ayalon, A., Matthews, A., Frumkin, A., Dayan, U., Halicz, L., Almogi-Labin, A., and Schilman, B., 2006, Paleoclimate and location of the border between Mediterranean climate region and the Saharo-Arabian Desert as revealed by speleothems from the northern Negev Desert, Israel: *Earth and Planetary Science Letters*, v. 249, p. 384–399, <https://doi.org/10.1016/j.epsl.2006.07.009>.
- Vaks, A., Bar-Matthews, M., Ayalon, A., Schilman, B., Gilmour, M., Hawkesworth, C.J., Frumkin, A., Kaufman, A., and Matthews, A., 2003, Paleoclimate reconstruction based on the timing of speleothem growth and oxygen and carbon isotope composition in a cave located in the rain shadow in Israel: *Quaternary Research*, v. 59, p. 182–193, [https://doi.org/10.1016/S0033-5894\(03\)00013-9](https://doi.org/10.1016/S0033-5894(03)00013-9).
- Vaks, A., Bar-Matthews, M., Matthews, A., Ayalon, A., and Frumkin, A., 2010, Middle-Late Quaternary paleoclimate of northern margins of the Saharan-Arabian Desert: reconstruction from speleothems of Negev Desert, Israel: *Quaternary Science Reviews*, v. 29, p. 2647–2662, <https://doi.org/10.1016/j.quascirev.2010.06.014>.
- Vaks, A., Woodhead, J., Bar-Matthews, M., et al., 2013a, Pliocene–Pleistocene climate of the northern margin of Saharan–Arabian Desert recorded in speleothems from the Negev Desert, Israel: *Earth and Planetary Science Letters*, v. 368, p. 88–100, <https://doi.org/10.1016/j.epsl.2013.02.027>.
- Vermeesch, P., 2018, IsoplotR: a free and open toolbox for geochronology: *Geoscience Frontiers*, v. 9, p. 1479–1493, <https://doi.org/10.1016/j.gsf.2018.04.001>.
- Zilberman, E., 1983, The geology of the central Sinai-Negev shear Zone, central Negev: Jerusalem, Israel, Geological Survey of Israel, Environmental Geology and Hydrogeology Division, p. 58.